

Thermodynamics of underdamped Brownian collisional engines: New insights and resonant phenomena

Gustavo A. L. Forão,¹ Fernando S. Filho,^{1,2} Bruno A. N. Akasaki,¹ and Carlos E. Fiore¹

¹Universidade de São Paulo, Instituto de Física, Rua do Matão, 1371, 05508-090 São Paulo, SP, Brazil

²UHasselt, Faculty of Sciences, Theory Lab, Agoralaan, 3590 Diepenbeek, Belgium

(Dated: July 2, 2024)

Collisional Brownian engines have been proposed as alternatives for nonequilibrium nanoscale engines. However, most studies have focused on the simpler overdamped case, leaving the role of inertia much less explored. In this work, we introduce the idea of collisional engines to underdamped Brownian particles, where each stage is sequentially subjected to a distinct driving force. A careful comparison between the performance of underdamped and overdamped Brownian work-to-work engines has been undertaken. The results show that underdamped Brownian engines generally outperform their overdamped counterparts. A key difference is the presence of a resonant regime in underdamped engines, in which both efficiency and power output are enhanced across a broad set of parameters. Our study highlights the importance of carefully selecting dynamics and driving protocols to achieve optimal engine performance.

The performance of engines and the search of protocol optimizations constitute fundamental issues in Thermodynamics since the seminal work by Sadi Carnot [1, 2] in 1872. Notwithstanding, the construction of different and reliable setups aimed at converting one kind of energy into another one has become more sophisticated, above all with the advent of the nanotechnology and new experimental procedures for investigating and creating nanoscale engines. Contrasting with macroscopic engines, fluctuations in nanoscale system can become important, making necessary the use of stochastic methods in order to obtain the thermodynamics properties and its relationship with the system performance. Stochastic thermodynamics (ST) [3–6] constitute an unified tool for describing nanoscale systems operating far from equilibrium [3–6] and tackling the role of fluctuation and dissipation.

Recently, a collisional (or sequential) description has been proposed and extended for Brownian systems [7–10]. In its simplest version, a single particle interacts sequentially with a thermal bath and is subjected to a specific work source at each stage. This approach differs from the situation where the system interacts with all thermal baths simultaneously [11, 12] and has been studied in distinct cases of non-equilibrium thermodynamics [13, 14], open quantum systems [14–17] and information and computational processing [14, 18–20]. Under suitable conditions, the sequential interaction operates as a heat engine or work-to-work converter, generating useful power. Despite this, its performance can be small or strongly reduced depending on the way it is designed, including the choice of ingredients such as period, temperatures, and the strength of driving worksources, revealing that the search of strategies and optimization routes as fundamental [7–9, 13, 21].

For describing the motion of particles in a colloidal environment subjected to random forces, a fundamental framework is the Langevin equation or Fokker-Planck approach [22, 23]. Its two employed variants, namely the underdamped and overdamped cases, capture distinct and essential aspects of particle dynamics and stochasticity. The underdamped variant emphasizes inertia and retains the correlation between particle and position, while the overdamped variant simplifies the

description and is suitable for systems with rapid relaxation. Despite the extensive research about them [24–31], little is known about their thermodynamic implications and the influence of inertial considerations on system performance and dissipation [11, 12].

In this paper, we advance upon previous works [7–10] by introducing and extending the concept of collisional Brownian engines to underdamped systems. For equal temperatures at each stage, we obtain exact expressions for Thermodynamic quantities such as work, heat and dissipation, solely expressed in terms of Onsager coefficients, irrespective the driving protocol. For distinct driving worksources, we provide a comparative study between underdamped and overdamped dynamics. The underdamped case is significantly different [7–10] due to the presence of a resonance phenomenon, resulting in a specific region on the phase space in which the engine operates at maximum power and maximum efficiency. The present study sheds light about the importance of dynamics and driving protocols for achieving optimal engine performances.

This paper is structured as follows: In Section I, we introduce the model, the main the expressions for the underdamped model and the maximization routes. In Section II, we compare the performance and dissipation of the engine ruled by each dynamic, as well as present the resonant phenomena in the Underdamped engine. Conclusions are drawn in Section III.

I. THERMODYNAMICS OF UNDERDAMPED BROWNIAN ENGINES

Our setup is composed of a Brownian particle sequentially placed in contact with a given thermal reservoir and subjected to a total force $\tilde{f}_i(x, t)$ per mass at each stage i , $i \in \{1, 2\}$. The former and latter contact has duration τ_1 and $\tau - \tau_1$, respectively, in which at each stroke i , the system dynamics is described by the equations,

$$\begin{cases} \frac{d}{dt} v_i(t) = \tilde{f}_i(x, t) - \gamma_i v_i(t) + \xi_i(t), \\ \frac{d}{dt} x_i(t) = v_i(t), \end{cases} \quad (1)$$

Here, γ_i represents the viscous coefficient per mass. The stochastic forces follow standard white noise properties: $\langle \xi_i(t) \rangle = 0$ and $\langle \xi_i(t) \xi_j(t') \rangle = 2\gamma_i k_B T_i \delta_{ij} \delta(t - t')/m$. The probability distribution of the particle $P_i(x, v, t)$ at the stroke i is described by Fokker-Planck-Kramers (FPK) [5, 7, 23, 32],

$$\frac{\partial P_i}{\partial t} = - \left[v \frac{\partial P_i}{\partial x} + \bar{f}_i(x, t) \frac{\partial P_i}{\partial v} + \frac{\partial J_i}{\partial v} \right], \quad (2)$$

where $\bar{f}_i(x, t)$ is decomposed in the following form $\bar{f}_i(x, t) = f_i^*(x) + \tilde{f}_i(t)$, where $f_i^*(x) = -\kappa x_i/m$ depends on the position, and $\tilde{f}_i(t)$ is time dependent and J_i is a current of probability given by

$$J_i = -\gamma_i v P_i - \frac{\gamma_i k_B T_i}{m} \frac{\partial P_i}{\partial v}. \quad (3)$$

At $t = \tau_1$, the particle switches to a second thermal bath at temperature T_2 and is subjected to a second force $\tilde{f}_2(x, t)$, which acts during $t \in [\tau_1, \tau]$. At $t = \tau$, a cycle is completed, and the particle returns to the first thermal bath with T_1 and $\tilde{f}_1(x, t)$, starting a new cycle. The collisional approach assumes the exchange of reservoirs happens instantaneously, effectively treating each switching as an adiabatic process. Some remarks about Eq. (2) are in order. First, the probability distribution has a Gaussian form regardless of the temperatures and drivings. Second, the specific case where $\tilde{f}_1(t) = \tilde{f}_2(t) = 0$ and the temperatures are equal, $T_1 = T_2$, corresponds to the Boltzmann-Gibbs distribution, describing the system in equilibrium thermodynamics. Third, even when $T_1 \neq T_2$ and/or $\tilde{f}_1(t) \neq \tilde{f}_2(t)$, the system evolves towards a nonequilibrium steady state (NESS). Lastly, to derive the model thermodynamics, we assume that both $P_i(v, x, t)$ and $J_i(v, x, t)$ vanish as $v \rightarrow \pm\infty$ and/or $x \rightarrow \pm\infty$. Therefore, the mean energy $U_i(t) = m\langle v_i^2 \rangle/2 + \kappa\langle x_i^2 \rangle/2$ has a time derivative expressed as the sum of two components,

$$\frac{d}{dt} U_i(t) = - \left[\dot{W}_i(t) + \dot{Q}_i(t) \right], \quad (4)$$

where the former and latter right terms denote the work (per time) done on the particle by the force $\tilde{f}_i(t)$ and the heat flux $\dot{Q}_i(t)$ exchanged with the thermal bath at the stroke i . Explicitly,

$$\dot{W}_i(t) = -m \langle v_i \rangle(t) \tilde{f}_i(t), \quad (5)$$

and

$$\dot{Q}_i(t) = \gamma_i \left(m \langle v_i^2 \rangle(t) - k_B T_i \right), \quad (6)$$

respectively. From now on, we shall curb ourselves for $\tau_1 = \tau/2$, whose external drivings can be expressed in the following form:

$$\tilde{f}_i(t) = \begin{cases} X_1 g_1(t), & 0 \leq t < \tau/2 \\ X_2 g_2(t), & \tau/2 \leq t < \tau, \end{cases} \quad (7)$$

where the X_i denotes the strength of the thermodynamic force per mass acting on the system, while $g_i(t)$ defines the shape

of the protocol. By evaluating (4) over a complete cycle and considering that the system returns to its initial state, one derives the first law of thermodynamics averaged over a period in NESS: $\bar{W}_1 + \bar{W}_2 + \bar{Q}_1 + \bar{Q}_2 = 0$. Similarly, the second law of thermodynamics relates to the time evolution of entropy $S_i = -k_B \langle \ln P_i \rangle$, which, together with Eq. (2), can be expressed through the difference between the entropy production rate $\sigma_i(t)$ and the entropy flux $\Phi_i(t)$:

$$\frac{d}{dt} S_i = \sigma_i(t) - \Phi_i(t), \quad (8)$$

where

$$\sigma_i(t) = \frac{m}{\gamma_i T_i} \int \frac{J_i^2}{P_i} dx dv \quad \text{and} \quad \Phi_i(t) = \frac{\dot{Q}_i(t)}{T_i}. \quad (9)$$

It is straightforward that $\sigma_i(t) \geq 0$, in accordance with the second law of Thermodynamics. By evaluating the entropy S_i over the complete period, one has that $\bar{\sigma} = \bar{\Phi} = -(\bar{Q}_1/T_1 + \bar{Q}_2/T_2)$, where $\bar{\sigma} = \left(\int_0^{\tau_1} \sigma_1(t) dt + \int_{\tau_1}^{\tau} \sigma_2(t) dt \right) / \tau$ and $\bar{\Phi} = \left(\int_0^{\tau_1} \Phi_1(t) dt + \int_{\tau_1}^{\tau} \Phi_2(t) dt \right) / \tau$. We can also relate $\bar{\sigma}$ with components \bar{Q}_i 's and \bar{W}_i 's by means of the following expression

$$\bar{\sigma} = \frac{4T^2}{4T^2 - \Delta T^2} \left[\frac{-(\bar{W}_1 + \bar{W}_2)}{T} + \frac{(\bar{Q}_1 - \bar{Q}_2)\Delta T}{2T^2} \right], \quad (10)$$

where we introduced the variables $T = (T_1 + T_2)/2$ and $\Delta T = T_1 - T_2$ together the first law of Thermodynamics. Since one of our goals is to compare overdamped and underdamped setups, we shall focus on the simplest case, in which temperatures are equal ($\Delta T = 0$) and the system presents only two thermodynamic forces, closely related with X_1 and X_2 . By adjusting X_1 and X_2 , such system can operate as work-to-work converters, generating useful power output during one of the two strokes. There are numerous examples of Brownian engines and biological physics operating as work-to-work converters [3, 26, 27, 33–36], where an amount of energy (e.g. chemical or mechanical) is converted into power output.

In this case, the Eq. (10) reduces to

$$\bar{\sigma} = \frac{-(\bar{W}_1 + \bar{W}_2)}{T}. \quad (11)$$

In order to exploit the driving changes at each stroke, we express $g_i(t)$ in terms of its Fourier components. More specifically,

$$g_1(t) = \frac{a_0}{2} + \sum_{n=1}^{\infty} a_n \cos\left(\frac{2\pi n t}{\tau}\right) + b_n \sin\left(\frac{2\pi n t}{\tau}\right), \quad (12)$$

and

$$g_2(t) = \frac{c_0}{2} + \sum_{n=1}^{\infty} c_n \cos\left(\frac{2\pi n t}{\tau}\right) + d_n \sin\left(\frac{2\pi n t}{\tau}\right), \quad (13)$$

respectively, where the driving to be considered is characterized by obtaining the coefficients a_n, b_n, c_n , and d_n under the conditions $c_n = d_n = 0$ for $i = 1$ and $a_n = b_n = 0$ for $i = 2$. It is worth mentioning that the Fourier representation ensures the boundary conditions with respect to the probability continuity at $t = \tau/2$ taking into account the system returns to the initial state at $t = \tau$. By averaging Eqs. (1), one finds the following general expression for $\langle v \rangle(t)$

$$\begin{aligned} \langle v \rangle(t) = & \sum_{k=1}^{\infty} (X_1 \cdot a_{1vk} + X_2 \cdot a_{2vk}) \cos\left(\frac{2\pi k t}{\tau}\right) \\ & + (X_1 \cdot b_{1vk} + X_2 \cdot b_{2vk}) \sin\left(\frac{2\pi k t}{\tau}\right), \end{aligned} \quad (14)$$

where a_{ivk} and b_{ivk} correspond to Fourier coefficients obtained for the mean velocity and depend on the driving form from Eqs. (12)-(13). Its explicit form is shown in the Appendix A. By plugging Eq. (14) into Eq. (5) and averaging over the duration of each stroke, one has \bar{W}_1 and \bar{W}_2 given by

$$\bar{W}_1 = -T J_1 f_1 = -T(L_{11} f_1^2 + L_{12} f_1 f_2), \quad (15)$$

$$\bar{W}_2 = -T J_2 f_2 = -T(L_{22} f_2^2 + L_{21} f_2 f_1), \quad (16)$$

expressed in terms of thermodynamic forces $f_i = X_i/T$ ($i \in \{1, 2\}$) and L_{ij} 's denote Onsager coefficients, whose main expressions are listed in Appendix A. Note that Eq. (10) can be re-expressed in terms of Onsager coefficients (in the regime of small ΔT) as $\bar{\sigma} \approx J_1 f_1 + J_2 f_2 + J_T f_T$, with $J_T = L_{TT} f_T$ and $f_T = \Delta T/T^2$ and L_{TT} is the associated Onsager coefficient. Since we are focused on the isothermal case, $f_T = 0$. Besides, in similarity with the overdamped case, there is no coupling between work fluxes and heat flux, implying that $L_{1T} = L_{T1} = L_{2T} = L_{T2} = 0$, consistent with the fact that such class of engines solely operates as work-to-work converters, rather than converting heat into work output.

In order the system can operate as a work-to-work converter, it is required an amount of $\bar{W}_{in} = \bar{W}_i$ be partially converted into work output $\mathcal{P} = \bar{W}_{out} = \bar{W}_j$, where $\mathcal{P} \geq 0 > \bar{W}_{in}$. The efficiency of conversion is thus given by

$$\eta \equiv -\frac{\mathcal{P}}{\bar{W}_{in}}, \quad (17)$$

where $0 \leq \eta \leq 1$. Notice that, for certain ranges of parameters, \bar{W}_j can be greater than \bar{W}_i , only meaning that in such case the amount of work $\bar{W}_{in} = \bar{W}_j$ is partially converted into $\bar{W}_{out} = \bar{W}_i$ and hence ($\tilde{f}_i \leftrightarrow \tilde{f}_j \Rightarrow \bar{W}_{in} \leftrightarrow \bar{W}_{out}$), solely implying that $\eta \leftrightarrow 1/\eta$. This change of regime is better exploited in Appendix B. When expressed in terms of Onsager coefficients and the thermodynamic forces, η is given by

$$\eta = -\frac{J_j f_j}{J_i f_i} = -\frac{L_{jj} f_j^2 + L_{ji} f_i f_j}{L_{ii} f_i^2 + L_{ij} f_j f_i}. \quad (18)$$

A. Overview about system maximizations

There are distinct routes for the optimization of power and efficiency in Brownian work-to-work converters. As stated in previous works [8, 9, 11], it is possible to express their optimized values in terms of Onsager coefficients. In this section, we briefly review them. Starting with the power and considering that f_i is held fixed, the engine regime is constrained between $0 < f_j < |f_m|$, where $f_m = -L_{ji} f_i / L_{jj}$. The force f_j^{MP} ensuring maximum power \mathcal{P}_{MP} is given by $f_j^{\text{MP}} = -L_{ji} f_i / 2L_{jj}$. By inserting this relation into Eqs. (16) and (18), one obtains the following expressions for quantities at maximum power:

$$\mathcal{P}_{\text{MP}} = T \frac{L_{ji}^2}{4 L_{jj}} f_i^2, \quad \eta_{\text{MP}} = \frac{L_{ji}^2}{4 L_{jj} L_{ii} - 2 L_{ji} L_{ij}}. \quad (19)$$

Conversely, one can search for f_j^{ME} by optimizing the efficiency with respect to f_j .

$$f_j^{\text{ME}} = \frac{L_{ii}}{L_{ij}} \left(-1 + \sqrt{1 - \frac{L_{ji} L_{ij}}{L_{jj} L_{ii}}} \right) f_i, \quad (20)$$

and

$$\eta_{\text{ME}} = -\frac{L_{ji}}{L_{ij}} + \frac{2L_{ii} L_{jj}}{L_{ij}^2} \left(1 - \sqrt{1 - \frac{L_{ij} L_{ji}}{L_{ii} L_{jj}}} \right), \quad (21)$$

and \mathcal{P}_{ME} is obtained by inserting f_j^{ME} into the expression for \mathcal{P} , respectively.

II. RESULTS

Unless it has been explicitly stated, we shall adopt $k_B = m = 1$, $\gamma_1 = \gamma_2 = \gamma$. Along this section, we draw a comparison between underdamped and overdamped Brownian engines for distinct driving forces. Our analysis assumes a constant (square wave) driving, given by $g_1(t) = g_2(t) = 1$, and a linear (sawtooth) driving, given by

$$g_i(t) = \begin{cases} \lambda t, & 0 \leq \lambda t \leq \tau/2 \\ \lambda(t - \tau/2) & \tau/2 \leq t \leq \tau, \end{cases} \quad (22)$$

where λ is a constant introduced in such a way $g_i(t)$ is dimensionless. In all cases we set $\lambda = 1$. We also investigate sinusoidal driving at each stage, as can be seen in the Appendix C. Fourier components of each driving protocol can be found in Appendix A.

A. Dynamics Comparison: Performance Contrast

In order to obtain a first insight about the similarities and differences between underdamped and overdamped collisional Brownian engines, Fig. 1 depicts, for distinct periods τ 's, the power and efficiency versus the force $X_2 = T f_2$ for

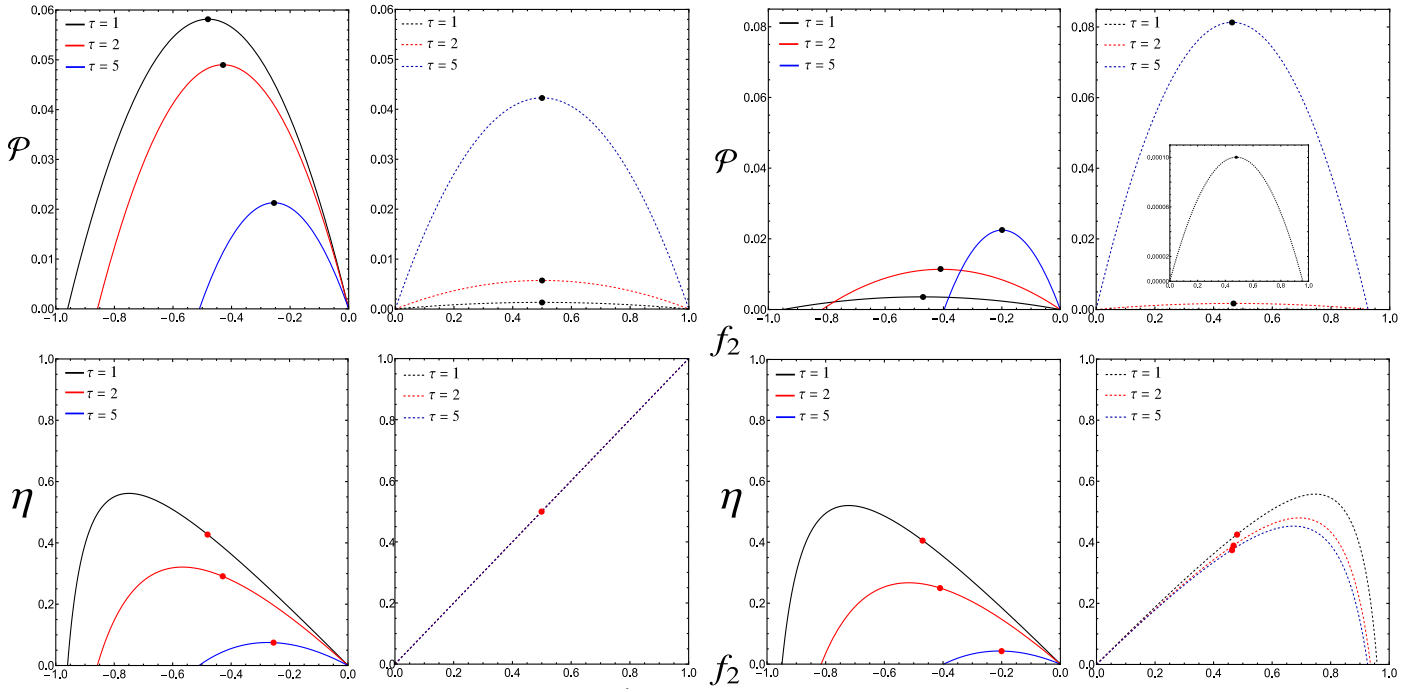


FIG. 1. Depiction of the power-output \mathcal{P} (top) and efficiency η (bottom) as functions of f_2 for constant (left) and linear (right) drivings and different periods τ . Dashed and continuous lines are for the underdamped and overdamped regimes, respectively. Black and red dots represent \mathcal{P}_{MP} and η_{MP} , respectively. Parameters: $f_1 = T = 1$, $\gamma = 1$ and $\kappa = 1$.

constant and linear drivings. For simplifying matters, such first sort of analysis will be carried out for $\gamma = \kappa = 1$. In both cases, the system can operate as a work-to-work converter by choosing f_2 constrained between 0 and $|f_m|$. We point out some remarkable differences between them, which can be understood by resorting to Onsager coefficients. For the (underdamped) constant protocol, expressions for Onsager coefficients listed in Appendix A show that $L_{11} = L_{22} = -L_{12} = -L_{21}$. As a consequence, the engine regime is delimited by $0 \leq f_2 \leq f_m = f_1$ (for all values of τ), and both \mathcal{P} and η acquire simple forms, given by $\mathcal{P} = L_{22}f_2(f_2 - f_1)$ and $\eta = f_2/f_1$, respectively, such latter solely depending on the ratio between forces, followed by maximum efficiency and power points yielding at $f_2^{ME} = f_1$ and $f_2^{MP} = f_1/2$, respectively, irrespective the values of κ, ω and τ . Maximum values read $\eta_{MP} = 1/2, \eta_{ME} = 1, \mathcal{P}_{MP} = TL_{22}f_1^2/4$ promptly obtained from Eqs. (19)-(21). While the former two are independent on the period, there is an optimal τ providing maximum \mathcal{P}_{MP} because L_{ij} 's exhibit a non monotonous behavior as τ is raised. In particular, for the sort of parameters it is peaked at $\tau_o = 6.311\dots$, whose maximum $\mathcal{P}_{MP} = 0.05148$. All such features are quite different from the overdamped case whose engine regime is strongly dependent on τ in which both power and efficiencies decrease as τ is raised (see e.g. left panels). Conversely, \mathcal{P}_{MP} decreases as τ is raised for the overdamped case.

The linear case is more revealing. Although Onsager coefficients also satisfy the relations $L_{11} = L_{22}$ and $L_{12} = L_{21}$, one has $L_{11} \neq -L_{12}$, and L_{11}/L_{22} increases “faster” than L_{12}/L_{21} as τ is raised. As a first consequence, f_m behaves differently

from the constant case and smoothly decreases as τ is raised. Also, $\mathcal{P}_{MP}, \eta_{MP}, \mathcal{P}_{ME}$ and η_{ME} are also differently from the constant case and depend on the interplay between κ and τ . For $\kappa = f_1 = 1$, \mathcal{P}_{MP} is maximum for $\tau_o = 7.345\dots$ whose associate power and efficiency are given by $\mathcal{P}_{MP} = 0.170\dots$ and $\eta_{MP} = 0.2765\dots$, respectively. The existence of an optimal τ_o ensuring maximum \mathcal{P}_{MP} also yields in the overdamped case, yielding at $\tau_o = 4.695\dots$ with a lower maximum power $\mathcal{P}_{MP} = 0.0224\dots$ (evaluated for $f_1 = \gamma = 1$).

Above findings can be understood in terms of some heuristic (no rigorous) arguments. We first note that, for a given protocol, strength driving forces in overdamped and underdamped cases operate at opposite and same directions in the work-to-work regime, respectively. This is due there is no need for an extra force to bring the system back to its initial position in the latter case, while in the former (overdamped) case, due to the absence of a restoring potential, it is essential for the system have two drivings acting in different directions in order to generate useful power. Such findings seem to be general and also verified for periodic protocols, but there are some subtleties for sinusoidal drivings, in part due to the phase difference between drivings (see Appendix C). Another difference between underdamped and overdamped relies the interplay between f_m and τ . Although it can be understood directly from Onsager coefficients, our heuristic argument states that the mean velocity aligns to the external force in both stages (for the overdamped case) for sufficiently long periods and hence no useful power output is generated. This is quite different for the underdamped case, due to the influence of restoring force and its interplay with period and driving.

B. Deterministic Resonant Phenomena in Underdamped Dynamics

The presence of a restoring potential in the underdamped case results in a resonant phenomena when an external force drives on the system and can significantly influence the system performance and the behavior of thermodynamic quantities. Such phenomena shares some similarities with the so called Stochastic Resonance (SR), verified recently in an experimental probe containing interacting resonant Brownian [37]. In the present case, our goal is to study the effects of a deterministic resonance due to an external driving at each stroke.

We start this section by deriving the resonant κ_{res} in terms of the system's parameters. The external driving is also a periodic force with total period τ and frequency $\omega = 2\pi/\tau$. The k -th contribution to the Fourier series of the mean velocity (14) is expressed as:

$$\begin{aligned} \langle v(t) \rangle^{k\text{-th}} &= (X_1 \cdot a_{1vk} + X_2 \cdot a_{2vk}) \cos\left(\frac{2\pi k t}{\tau}\right) \\ &+ (X_1 \cdot b_{1vk} + X_2 \cdot b_{2vk}) \sin\left(\frac{2\pi k t}{\tau}\right). \end{aligned} \quad (23)$$

The resonant phenomenon is characterized by a maximum of amplitude of $\langle v(t) \rangle^{k\text{-th}}$ with respect to the time t and κ , described by the following relation.

$$\kappa_{\text{res}} = \left(\frac{2\pi k}{\tau}\right)^2, \quad k \text{ integer} \quad (24)$$

Such result is protocol-independent, solely depending on the natural frequency $\omega_0 = 2\pi/\tau$, and hence valid to a generic external driving. The relationship between resonance and the system performance is depicted in Fig. 2 for constant and linear drivings. We first note that it can remarkably influence the system performance, not only as forces f_1/f_2 are varied (not shown), but also for their optimized values $\mathcal{P}_{MP}/\eta_{MP}$ and $\mathcal{P}_{ME}/\eta_{ME}$ evaluated at $f_2 = f_2^{\text{MP}}$ and $f_2 = f_2^{\text{ME}}$, respectively. In both cases, resonances lines (continuous lines in heat maps) obey Eq. (24) and are followed by the increase of power and efficiency for constant and linear drivings for odd and any integer k , respectively. A direct inspection of Eq. (24) for constant drivings reveals that $\langle v(t) \rangle^{k\text{-th}} \ll 1$ for even k , leading to strongly small performances in such a case. Bottom left panels reinforce such findings for $\kappa = 4\pi^2$ in which $\tau_{\text{res}} = k$. Also, in accordance with that stated in the previous section, η_{MP} and η_{ME} are always constant in such case for constant protocols. As a complementar analysis, we also compare numerically the performances at the resonance and out of the resonance. For example, for $\tau = 5$, $\kappa_{\text{res}} = 4\pi^2/25$ and $\kappa = 1$, both constant (linear) drivings provide the system operates with larger performances in the resonance $\mathcal{P}_{MP} = 5, 12 \cdot 10^{-2}$ ($9, 91 \cdot 10^{-2}$) than out the resonance $\mathcal{P}_{MP} = 4, 23 \cdot 10^{-2}$ ($8, 12 \cdot 10^{-2}$), respectively, but in both cases, efficiencies are close to each other $\eta_{MP} = 1/2$ (0.38). Hence, the existence of resonance in the underdamped case can confer a remarkable advantage over the overdamped dynamics, not only because it is protocol-independent but also it can enhance power without sacrificing

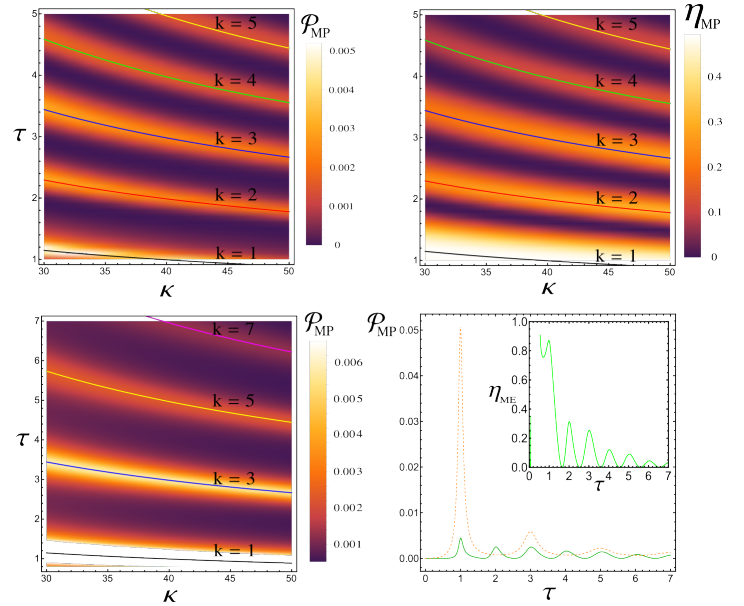


FIG. 2. Top panels: Depiction of the maximum power \mathcal{P}_{MP} (left) and efficiency at maximum power η_{MP} (right) heat maps for linear drivings. Left bottom panel show the same, but for constant drivings. Continuous lines show the resonance lines according to Eq. (24). All maximizations have been carried out with respect to f_2 . Since $\eta_{MP} = 1/2$ for constant drivings, heat maps in such case has not been shown. Right bottom panels: Plot of \mathcal{P}_{MP} for constant (dashed) and linear (continuous) drivings for $\kappa = 4\pi^2$. Inset: the same but for η_{ME} (linear). Parameters: $f_1 = T = 1$ and $\gamma = 1$.

efficiency. However, a common trait to all resonance patterns is that they are signed by increasing dissipation (see e.g. right panels in the Fig. 4). Similar findings are also viewed for harmonic drivings, as depicted in Appendix C for drivings dephased of π at each stroke. As a consequence, resonance lines and maximum \mathcal{P}_{MP} and η_{ME} are also half period translated (see e.g. Fig. 7). As a last comment, although resonances points are very close to the peaks of \mathcal{P}_{MP} and η_{ME} (inset), they do not precisely coincide (although differences typically yield at the third decimal level).

We close this section by estimating how resonant phenomena can be feasible from an experimental point of view. In principle, our framework might be tested experimentally in an optical tweezers systems, in which the harmonic potential and the external drives can be generated via controlled electric fields [38–41]. For that, we take some values for laboratory quantities: $m \approx 10^{-18}$ kg, $\gamma \approx 10^{-20} \text{s}^{-1}$ by imposing the thermodynamics force $X_1 \approx 0.003$ fN/kg in the underdamped case ($m/\gamma \gg 1$) and in room temperature with $\kappa \approx 1 \mu\text{N/m}$. For such values, the resonant regime is peaked at $X_2 \approx 0.5$ fN/kg in the period $\tau \approx 6 \mu\text{s}$ in the constant case. Fig. 3 depicts the heat maps for constant and linear protocols for parameters described above. As in Fig. (2), resonance positions are coincident in both constant and linear drivings, consistent to be protocol independent. Also in accordance to previous results, results linear drivings present more resonance lines. Although heat maps suggest that resonances can be experimentally ver-

ified, it requires a fine tuning of model parameters, indicating that a small perturbation of parameters (e.g. the time cycle and/or in the harmonic potential) can be drop the particle from the resonance region.

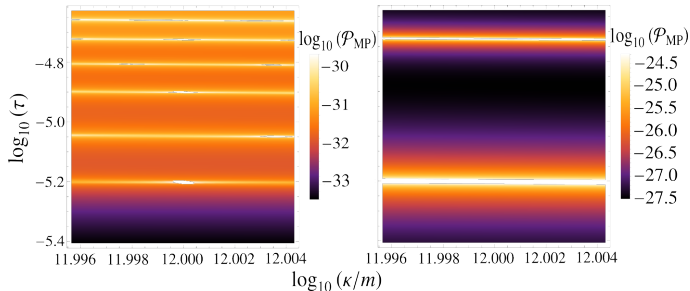


FIG. 3. The power output for the linear (left) and constant (right) protocols in log base 10 scale considering some experimental quantities. Here, we use $m \approx 10^{-18}$ kg and $\gamma \approx 10^{-20}$ s $^{-1}$.

C. Entropy Production

1. Dynamics Comparison and dissipation at resonant regimes

The entropy production serves as a key indicator of system dissipation, being investigated in distinct contexts, such as in the existence of different trade-offs between dissipation and fluctuation, expressed via TURs [42–45], its interplay or compromise with power and efficiency in the context of thermal engines [7–9, 46, 47] or even its usage for the characterization of phase transition regimes [48–50]. Despite it is commonly desired to minimizing entropy production and simultaneously maximizing power and/or efficiency, the second law of thermodynamics precludes all of them be simultaneously satisfied. With this in mind, this section is aimed at depicting the entropy production behavior of our collisional (underdamped Brownian) engine regimes, above all at the resonance regimes, as well as drawing a comparison with overdamped dynamics. In terms of Onsager coefficients, Eq. (11) acquires the form $\bar{\sigma} = L_{11}f_1^2 + L_{22}f_2^2 + (L_{12} + L_{21})f_1f_2$. In order to obtain a first insight, Fig. 9 depicts, for the same parameters as in Figs. 1 and 2, the behavior of entropy production $\bar{\sigma}$ versus f_2 and $\bar{\sigma}_{MP}$ heat maps, evaluated at $f_2 = f_2^{MP}$ respectively. Starting with constant protocol, it acquires a simple form $\bar{\sigma} = L_{22}(f_2 - f_1)^2$, meaning that its minimum value $\bar{\sigma}_{mS} = 0$ coincides the maximum efficiency point $f_2^{ME} = f_1$, irrespective the period and model parameters. This is different from the overdamped case, not only because $\bar{\sigma}_{mS}$ increases as τ is raised (overdamped) but also the underdamped case is characterized by $0 = \bar{\sigma}_{mS} \neq \bar{\sigma}_m > 0$ (for the overdamped case one has $\bar{\sigma}_m = \bar{\sigma}_{mS} > 0$). Another important comparison relies the behavior $\bar{\sigma}_{MP}$ and $\bar{\sigma}_{ME}$ (not shown). Both of them increase as τ is raised. However the underdamped case permits κ do be adjusted to control the dissipation rather than the overdamped case, or even to ensure the desirable compromise between power, efficiency and dissipation (e.g. for the parameters in Fig. 4, τ and κ can be adjusted for ensuring larger \mathcal{P} 's

and lower $\bar{\sigma}$'s).

Lastly, we address the consequences for the dissipation at the resonant regime, as depicted by the right panels of Fig. 4 for the same parameters as in Fig. 2. Resonance patterns are also manifested in the entropy production behavior. Apart from the explanation in terms of Onsager coefficients, we present an alternative argument for the constant protocol. Since $\eta_{MP} = 1/2$ implies that $\bar{W}_1 = -2\bar{W}_2$, the entropy production acquires the simple form $\bar{\sigma}_{MP} = \bar{W}_2/T$, meaning that dissipation heat maps behaves similarly to the power heat map, albeit by a factor T . Although above similar relation is not presented for the linear protocol, resonant patterns are still visible, but less pronounced than power output and efficiency heat maps. This is because entropy production in such cases assume values close to those out the resonance lines.

III. CONCLUSIONS

In this paper, we introduced a sequential engine description for underdamped Brownian engines in which the particle is subjected to distinct worksources at each stage. Exact thermodynamics quantities were obtained from the framework of stochastic thermodynamics. The influence of for distinct driving driving protocols and a detailed comparison with its overdamped dynamics was undertaken. Our findings highlighted remarkable advantages of the underdamped dynamics when compared with its overdamped counterpart, particularly in scenarios where minimizing dissipation while maximizing power is crucial. Despite the overdamped dynamics exhibiting superior performances in some specific cases, it is typically more dissipative, less efficient and presents inferior power outputs. Furthermore, the second main feature regarding underdamped case is the existence of resonance lines, which can significantly enhance the system performance. The resonance regime not only increases the power but also enables such enhancements without compromising efficiency. This underscores the role of such phenomena as a mechanism of optimizing the engine operation and opens possibilities for the development of efficient and versatile Brownian engines. Overall, our comparative analysis emphasizes the importance of carefully selecting dynamics and driving protocols to optimize engine performance.

ACKNOWLEDGMENTS

Authors acknowledge the financial support from FAPESP under grants 2021/03372-2 and 2022/16192-5.

Appendix A: General Fourier coefficients of the mean velocity and General Onsager coefficients

For the underdamped case, Fourier coefficients for the mean velocity, obtained via the solution of the system equations, are listed below:

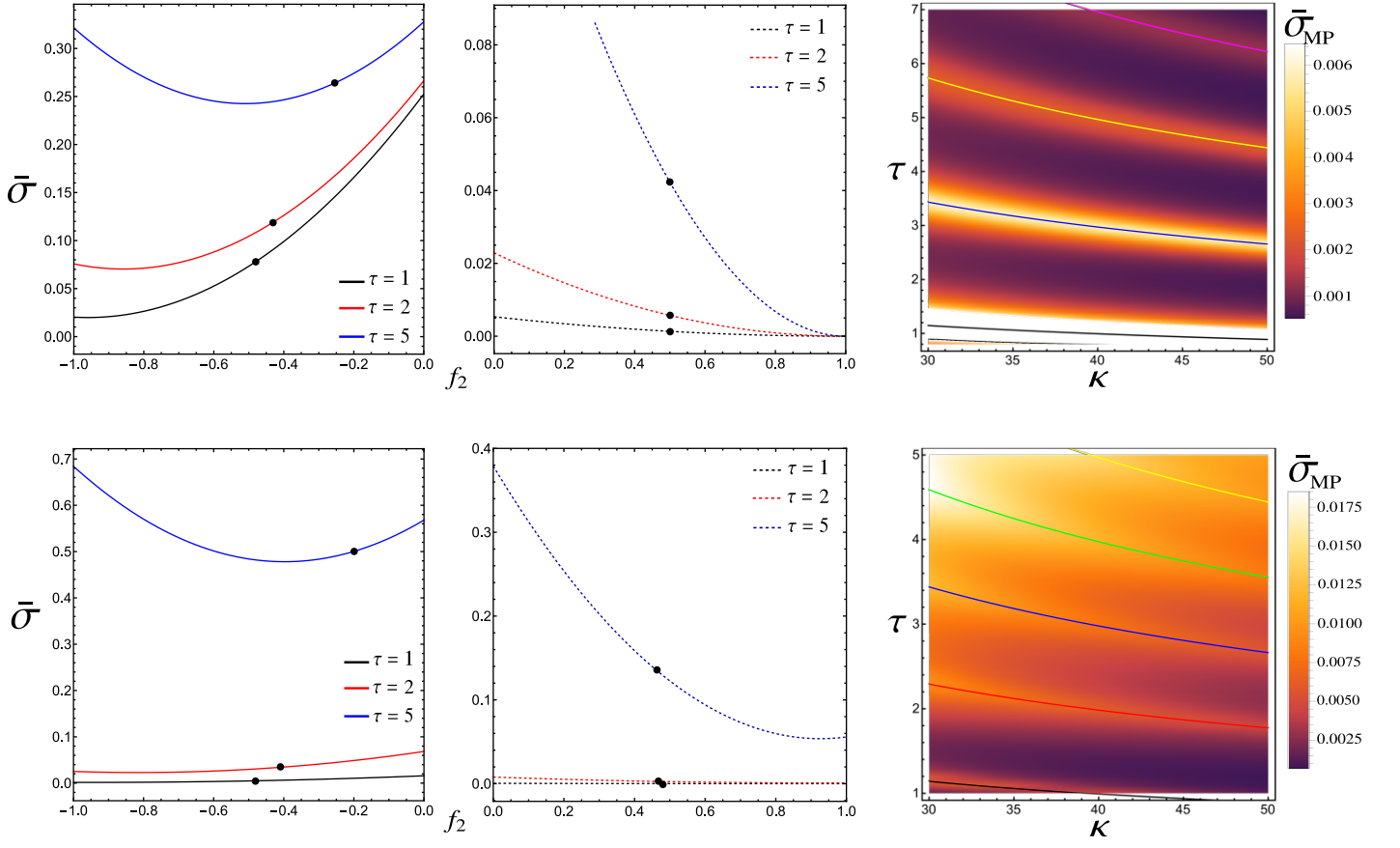


FIG. 4. Left and center panels depict the mean entropy production $\bar{\sigma}$ for the overdamped (left) and underdamped (center) versus f_2 for the same range, resonant lines and parameters as in Fig. (6). Black dots represents attempt to the maximum power. Right panels show entropy production heat maps for the same parameters from Fig. (2). Top and bottom panels attempt to the constant and linear drivings, respectively. Parameters: $f_1 = 1$, $\gamma = 1$ and $T = 1$ in all plots and $\kappa = 1$ for the 2D plots.

$$a_{1kv} = \frac{8\pi k\tau (8\pi\gamma k\tau a_n + b_n (\tau^2(\gamma^2 - \omega_D^2) - 16\pi^2 k^2))}{(\tau^2(\gamma - \omega_D)^2 + 16\pi^2 k^2)(\tau^2(\gamma + \omega_D)^2 + 16\pi^2 k^2)},$$

$$a_{2kv} = \frac{8\pi k\tau (8\pi\gamma k\tau c_n + d_n (\tau^2(\gamma^2 - \omega_D^2) - 16\pi^2 k^2))}{(\tau^2(\gamma - \omega_D)^2 + 16\pi^2 k^2)(\tau^2(\gamma + \omega_D)^2 + 16\pi^2 k^2)},$$

$$b_{1kv} = \frac{8\pi k\tau (a_n (\tau^2(\omega_D^2 - \gamma^2) + 16\pi^2 k^2) + 8\pi\gamma k\tau b_n)}{(\tau^2(\gamma - \omega_D)^2 + 16\pi^2 k^2)(\tau^2(\gamma + \omega_D)^2 + 16\pi^2 k^2)},$$

and

$$b_{2kv} = \frac{8\pi k\tau (c_n (\tau^2(\omega_D^2 - \gamma^2) + 16\pi^2 k^2) + 8\pi\gamma k\tau d_n)}{(\tau^2(\gamma - \omega_D)^2 + 16\pi^2 k^2)(\tau^2(\gamma + \omega_D)^2 + 16\pi^2 k^2)},$$

expressed in terms of Fourier coefficients a_n , b_n , c_n and d_n for $g_1(t)$ and $g_2(t)$, respectively, and $\omega_D = \sqrt{\gamma^2 - 4\kappa}$ is the damped oscillation frequency of the system. Onsager coefficients are related to coefficients a_{ikv} and b_{ikv} via the following expressions

$$L_{11} = T \sum_{n=1}^{\infty} \sum_{k=1}^{\infty} \frac{(\pi k a_{1kv} a_k - b_{1kv} (a_0 ((-1)^k - 1) - \pi k b_k))}{4\pi k} +$$

$$(1 - \delta_{n,k}) \cdot \left(-\frac{((-1)^{k+n} - 1) (k a_n b_{1kv} - n a_{1kv} b_n)}{2\pi (k^2 - n^2)} \right),$$

$$L_{12} = T \sum_{n=1}^{\infty} \sum_{k=1}^{\infty} \frac{(\pi k a_{2kv} a_k - b_{2kv} (a_0 ((-1)^k - 1) - \pi k b_k))}{4\pi k} +$$

$$(1 - \delta_{n,k}) \cdot \left(-\frac{((-1)^{k+n} - 1) (k a_n b_{2kv} - n a_{2kv} b_n)}{2\pi (k^2 - n^2)} \right),$$

$$L_{21} = T \sum_{n=1}^{\infty} \sum_{k=1}^{\infty} \frac{1}{4} \left(a_{1kv} c_k + \frac{c_0 ((-1)^k - 1) b_{1kv}}{\pi k} + b_{1kv} d_k \right) +$$

$$(1 - \delta_{n,k}) \cdot \left(\frac{((-1)^{k+n} - 1) (k b_{1kv} c_n - n a_{1kv} d_n)}{2\pi (k^2 - n^2)} \right),$$

and

$$L_{22} = T \sum_{n=1}^{\infty} \sum_{k=1}^{\infty} \frac{1}{4} \left(a_{2kv} c_k + \frac{c_0 ((-1)^k - 1) b_{2kv}}{\pi k} + b_{2kv} d_k \right) +$$

$$(1 - \delta_{n,k}) \cdot \left(\frac{((-1)^{k+n} - 1) (k b_{2kv} c_n - n a_{2kv} d_n)}{2\pi (k^2 - n^2)} \right).$$

For constant and linear drivings, coefficients a_n, b_n, c_n and d_n 's are listed below:

$$a_0 = c_0 = 1, \quad a_n = c_n = 0, \quad b_n = -d_n = \frac{-1 + (-1)^n}{\pi n}, \quad (\text{A1})$$

for constant drivings and

$$a_0 = c_0 = \tau/4, \quad a_n = -c_n = \frac{((-1)^n - 1)\tau}{2\pi^2 n^2}, \quad d_n = -\frac{\tau}{2\pi n}, \quad (\text{A2})$$

and $b_n = (-1)^n d_n$ for linear drivings, respectively. For harmonic drivings, Fourier coefficients read $a_1 = d_1 = 1/2$, $a_n = d_n = 0 \forall n \neq 1$, $b_1 = c_1 = 0$, $b_n = (1 + (-1)^n)n/((n^2 - 1)\pi) = n \cdot c_n \forall n \neq 1$ and $c_0 = -2/\pi$. By inserting them into expressions for $a_{1kv}, a_{2kv}, b_{1kv}$ and b_{2kv} , Onsager coefficients can be promptly evaluated.

For the sake of completeness, we also list Onsager coefficients for the overdamped case [8]:

$$L_{11} = 1 - \frac{2}{\gamma\tau} \tanh\left(\frac{\gamma\tau}{4}\right), \quad (\text{A3})$$

and

$$L_{12} = \frac{2}{\gamma\tau} \tanh\left(\frac{\gamma\tau}{4}\right), \quad (\text{A4})$$

for constant drivings, where $L_{11} = L_{22}$ and $L_{12} = L_{21}$ and

$$L_{11} = \frac{1}{12\gamma\tau} \left\{ \gamma^3 \tau^3 - 3(\gamma^2 \tau^2 - 8) \coth\left(\frac{\gamma\tau}{2}\right) - 24 \text{csch}\left(\frac{\gamma\tau}{2}\right) \right\} \quad (\text{A5})$$

and

$$L_{12} = \frac{(-\gamma\tau + 2e^{\frac{\gamma\tau}{2}} - 2)(e^{\frac{\gamma\tau}{2}}(\gamma\tau - 2) + 2)}{2\gamma\tau(e^{\gamma\tau} - 1)} \quad (\text{A6})$$

for the linear drivings, respectively, where $L_{22} = L_{11}$ and $L_{12} = L_{21}$.

Appendix B: Distinct engine operation regimes

As discussed before in the main text, the interplay among parameters can generate two worksources with opposite signals, $\bar{W}_{\text{in}} < 0$ and $\bar{W}_{\text{out}} > 0$, representing the conversion of

one energy (per time) into another one, the latter being identified as the power-output. However, an interesting feature in both overdamped and underdamped cases, relies to the fact the increase of driving strength f_2 and f_1 held fixed (analogously for the other way around) can change the regime operation. This is depicted in Fig. 5 by plotting $\bar{W}_1 \leftrightarrow \bar{W}_2$ as f_2 is changed. From Eqs. (5) and (15) and equal $L_{12} = L_{21}$ (the all cases here) we see that the change of regime yields at $f_2^* = \pm \sqrt{L_{11}/L_{22}f_1}$, whose efficiency is given by $\eta = -\bar{W}_1/\bar{W}_2$ for $f_2 < f_2^*$ and $1/\eta$ for $f_2 > f_2^*$, respectively. Since $L_{11} = L_{22}$ for constant and linear drivings and $f_1 = 1$ is held fixed, \bar{W}_1 presents a linear behavior, whether operating as \bar{W}_{in} or \bar{W}_{out} , whose crossover of regimes yields at $f_2^* = -1$ and $f_2^* = 1$ for the overdamped and underdamped cases, respectively. As a last comment, taking into account that the efficiency is given by the ratio between \bar{W}_{out} and \bar{W}_{in} the crossover between regimes is characterized by infinitely large values of η (gray lines), in similarity with previous works [51].

Appendix C: Sinusoidal harmonic drivings

Sinusoidal driving forces appears in several contexts, such as for modelling Brownian particles under optical beam traps and optical tweezers [38–41], electrophoresis process in colloidal gels [52] or even by measuring heat capacity experimentally by means of oscillating temperatures [53, 54]. In this Appendix we reproduces aforementioned features for harmonic drivings given by

$$\tilde{f}_i(t) = \begin{cases} X_1 \cos\left(\frac{2\pi}{\tau}t\right), & 0 \leq t \leq \tau/2 \\ X_2 \sin\left(\frac{2\pi}{\tau}t\right), & \tau/2 \leq t \leq \tau. \end{cases} \quad (\text{C1})$$

Fig. (6) summarizes the main findings for the underdamped (right) and overdamped (left) panels. While \mathcal{P} increases as τ is raised (overdamped), the opposite trend is verified for the associated efficiencies and for underdamped case. In similarity with constant and linear drivings, the underdamped case not only presents substantial larger efficiencies and power-outputs than the overdamped case but also yields a substantially larger operation regime.

As stated in the main text, resonant effects for sinusoidal drivings also improves the power and efficiency, but does not show remarkable improvements with respect to constant and linear drivings.

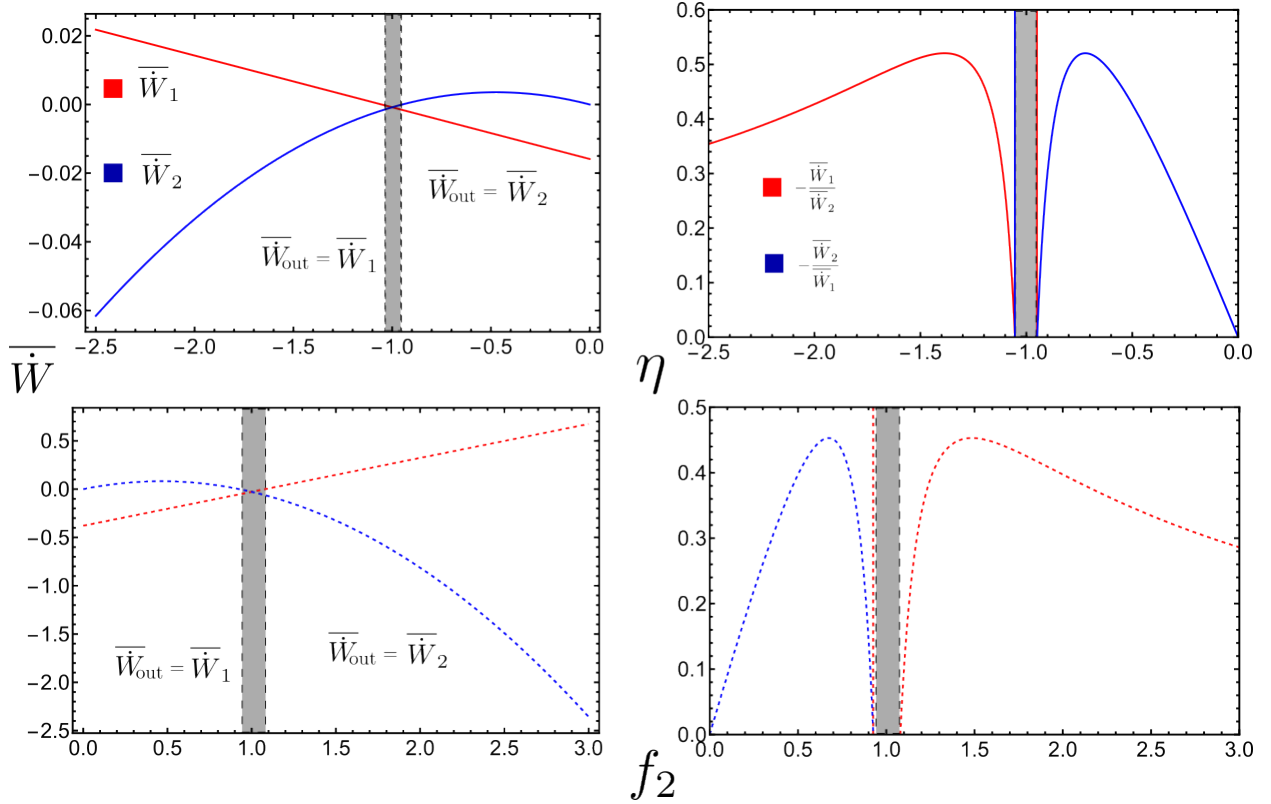


FIG. 5. Depiction of average powers $\overline{W}_1, \overline{W}_2$ (left) and efficiencies (right) for the overdamped (top continuous line) and for the underdamped (bottom dashed lines) for $f_1 = 1$. For better visualization, we adopted $\tau = 1$ in the overdamped case and $\tau = 5$ for the underdamped case. The dashed black lines represent the points where the exchange of fluxes $\overline{W}_{\text{out}} \leftrightarrow \overline{W}_{\text{in}}$ occurs and the gray region represents a “dud” regime.

-
- [1] S. Carnot, in *Annales scientifiques de l'École normale supérieure*, Vol. 1 (1872) pp. 393–457.
- [2] M. J. De Oliveira et al., *Equilibrium thermodynamics* (Springer, 2013).
- [3] U. Seifert, *Reports on progress in physics* **75**, 126001 (2012).
- [4] C. Van den Broeck and M. Esposito, *Physica A: Statistical Mechanics and its Applications* **418**, 6 (2015), proceedings of the 13th International Summer School on Fundamental Problems in Statistical Physics.
- [5] T. Tomé and M. J. de Oliveira, *Phys. Rev. E* **82**, 021120 (2010).
- [6] T. T. M. d. Castro and M. J. d. Oliveira, *Journal of Chemical Physics* (2018), 10.1063/1.5037045.
- [7] A. L. L. Stable, C. E. F. Noa, W. G. C. Oropesa, and C. E. Fiore, *Phys. Rev. Res.* **2**, 043016 (2020).
- [8] C. E. F. Noa, A. L. L. Stable, W. G. C. Oropesa, A. Rosas, and C. E. Fiore, *Phys. Rev. Res.* **3**, 043152 (2021).
- [9] F. S. Filho, B. A. N. Akasaki, C. E. F. Noa, B. Cleuren, and C. E. Fiore, *Phys. Rev. E* **106**, 044134 (2022).
- [10] I. N. Mamede, A. L. L. Stable, and C. E. Fiore, *Phys. Rev. E* **106**, 064125 (2022).
- [11] K. Proesmans, Y. Dreher, M. c. v. Gavrilov, J. Bechhoefer, and C. Van den Broeck, *Phys. Rev. X* **6**, 041010 (2016).
- [12] K. Proesmans and C. Van den Broeck, *Chaos: An Interdisciplinary Journal of Nonlinear Science* **27** (2017).
- [13] A. Rosas, C. Van den Broeck, and K. Lindenberg, *Phys. Rev. E* **96**, 052135 (2017).
- [14] J. M. Parrondo, J. M. Horowitz, and T. Sagawa, *Nature physics* **11**, 131 (2015).
- [15] F. L. S. Rodrigues, G. De Chiara, M. Paternostro, and G. T. Landi, *Phys. Rev. Lett.* **123**, 140601 (2019).
- [16] P. Strasberg, G. Schaller, T. Brandes, and M. Esposito, *Phys. Rev. X* **7**, 021003 (2017).
- [17] O. A. D. Molitor and G. T. Landi, *Phys. Rev. A* **102**, 042217 (2020).
- [18] T. Sagawa, *Journal of Statistical Mechanics: Theory and Experiment* **2014**, P03025 (2014).
- [19] K. Maruyama, F. Nori, and V. Vedral, *Rev. Mod. Phys.* **81**, 1 (2009).
- [20] C. H. Bennett, *International Journal of Theoretical Physics* **21**, 905 (1982).
- [21] P. E. Harunari, F. S. Filho, C. E. Fiore, and A. Rosas, *Phys. Rev. Res.* **3**, 023194 (2021).
- [22] N. G. Van Kampen, *Stochastic processes in physics and chemistry*, Vol. 1 (Elsevier, 1992).
- [23] T. Tomé and M. J. De Oliveira, *Stochastic dynamics and irreversibility* (Springer, 2015).
- [24] J. Tóthová and V. Lisý, *European Journal of Physics* **43**, 065103 (2022).
- [25] H. Safdari, A. G. Cherstvy, A. V. Chechkin, A. Bodrova, and R. Metzler, *Phys. Rev. E* **95**, 012120 (2017).
- [26] M. F. K. Pebeu, R. L. Woulaché, and T. C. Kofane, *Phys. Rev. E* **98**, 052107 (2018).

- [27] M. E. Fisher and A. B. Kolomeisky, Proceedings of the National Academy of Sciences **96**, 6597 (1999).
- [28] S. Leibler, Nature **370** (1994).
- [29] A. S. Bodrova, A. V. Chechkin, A. G. Cherstvy, H. Safdari, I. M. Sokolov, and R. Metzler, Scientific reports **6**, 30520 (2016).
- [30] P. Nazé, S. Deffner, and M. V. Bonança, Journal of Physics Communications **6**, 083001 (2022).
- [31] S. De Karmakar and R. Ganesh, Physical Review E **101**, 032121 (2020).
- [32] C. Van den Broeck and M. Esposito, *Phys. Rev. E* **82**, 011144 (2010).
- [33] D. M. Busiello and C. Fiore, Journal of Physics A: Mathematical and Theoretical **55**, 485004 (2022).
- [34] S. Liepelt and R. Lipowsky, Physical review letters **98**, 258102 (2007).
- [35] S. Liepelt and R. Lipowsky, Physical Review E **79**, 011917 (2009).
- [36] H. Hooyberghs, B. Cleuren, A. Salazar, J. O. Indekeu, and C. Van den Broeck, The Journal of chemical physics **139** (2013).
- [37] Y. Luo, C. Zeng, and B. Li, Europhysics Letters **137**, 21002 (2022).
- [38] B. Suassuna, B. Melo, and T. Guerreiro, *Phys. Rev. A* **103**, 013110 (2021).
- [39] L. P. Ghislain, N. A. Switz, and W. W. Webb, Review of Scientific Instruments **65**, 2762 (1994).
- [40] T. Davis, Optics express **15**, 2702 (2007).
- [41] M. J. Padgett, J. Molloy, and D. McGloin, *Optical Tweezers: methods and applications* (CRC press, 2010).
- [42] A. C. Barato and U. Seifert, Physical review letters **114**, 158101 (2015).
- [43] S. Otsubo, S. Ito, A. Dechant, and T. Sagawa, Physical Review E **101**, 062106 (2020).
- [44] Y. Hasegawa and T. Van Vu, Physical Review E **99**, 062126 (2019).
- [45] K. Proesmans and C. Van den Broeck, Europhysics Letters **119**, 20001 (2017).
- [46] K. Proesmans, B. Cleuren, and C. Van den Broeck, *Phys. Rev. Lett.* **116**, 220601 (2016).
- [47] I. N. Mamede, P. E. Harunari, B. A. N. Akasaki, K. Proesmans, and C. E. Fiore, *Phys. Rev. E* **105**, 024106 (2022).
- [48] C. E. F. Noa, P. E. Harunari, M. J. de Oliveira, and C. E. Fiore, *Phys. Rev. E* **100**, 012104 (2019).
- [49] M. Aguilera, M. Igarashi, and H. Shimazaki, Nature Communications **14**, 3685 (2023).
- [50] S. A. Loos, S. H. Klapp, and T. Martynek, Physical review letters **130**, 198301 (2023).
- [51] F. S. Filho, G. A. L. Forão, D. M. Busiello, B. Cleuren, and C. E. Fiore, *Phys. Rev. Res.* **5**, 043067 (2023).
- [52] G. W. Slater, P. Mayer, and P. D. Grossman, Electrophoresis **16**, 75 (1995).
- [53] G. W. H. Höhne, W. Hemminger, H.-J. Flammersheim, et al., *Differential scanning calorimetry*, Vol. 2 (Springer, 2003).
- [54] L. Filippov, International Journal of Heat and Mass Transfer **9**, 681 (1966).

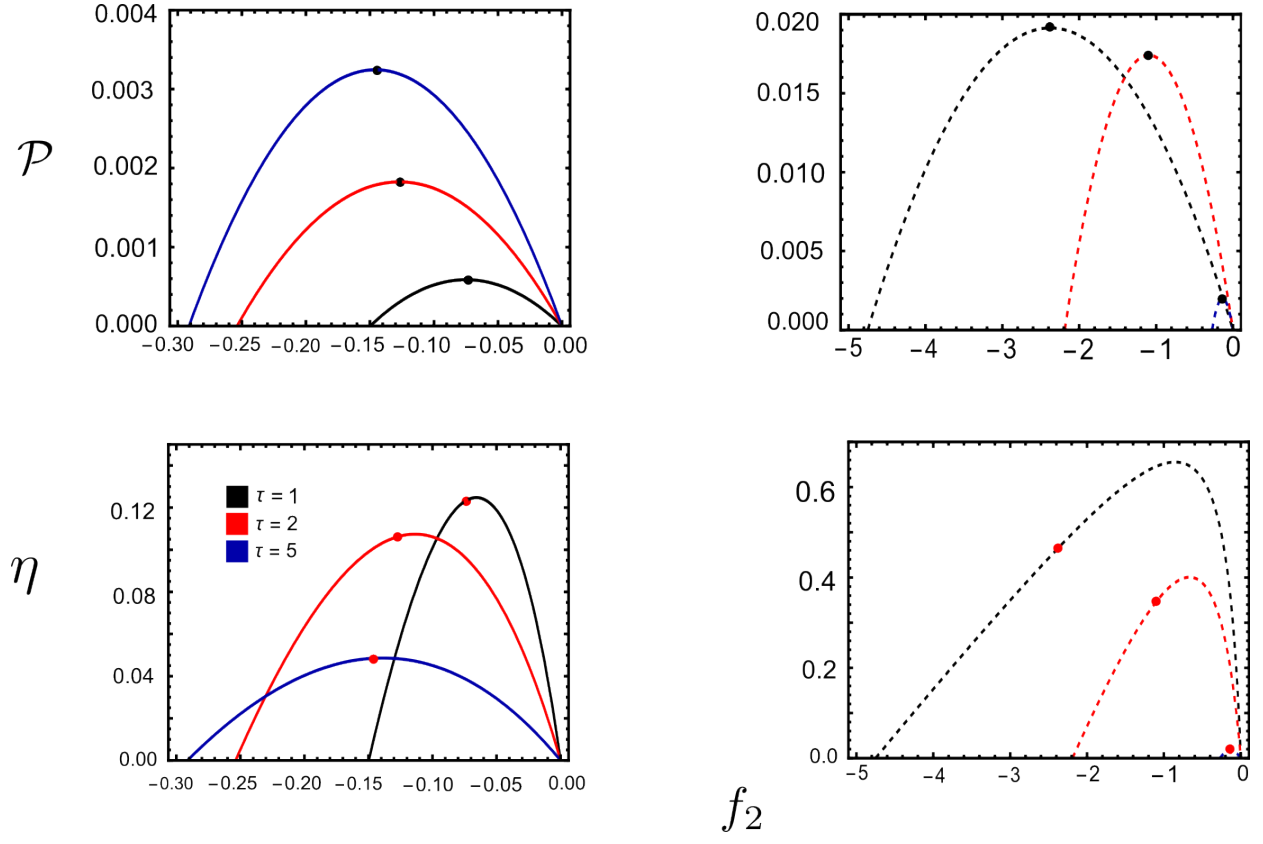


FIG. 6. Power-output (top) and efficiency (bottom) versus f_2 for sinusoidal protocols and various periods τ . Dashed lines represent the underdamped regime, while continuous lines represent the overdamped regime. Black bullets are \mathcal{P}_{MP} and red bullets are η_{MP} . Parameters: $f_1 = 1$, $\gamma = 1$ and $\kappa = 1$.

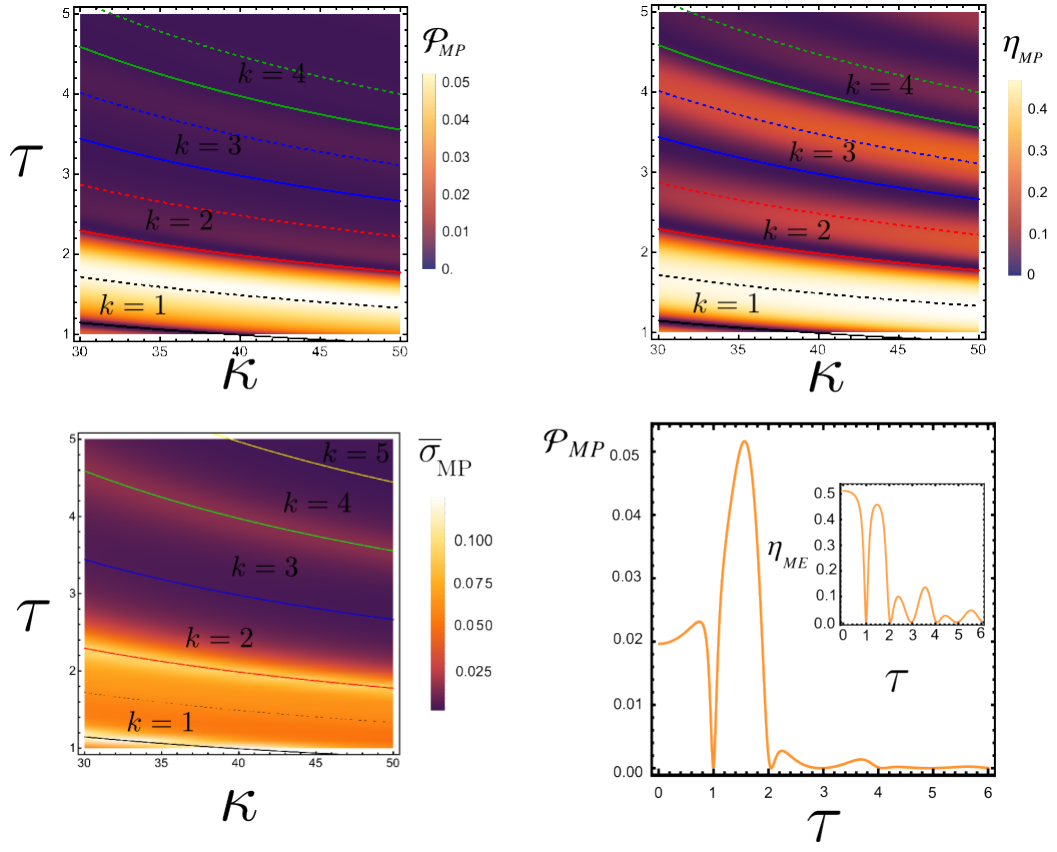


FIG. 7. Depiction of \mathcal{P}_{MP} , η_{MP} and $\bar{\sigma}_{MP}$ heat maps for harmonic drivings. Right bottom panels show \mathcal{P}_{MP} and η_{ME} (inset) for $\kappa = 4\pi^2$. Parameters: f_1 and $\gamma = 1 = T = 1$.